Supplement of Atmos. Chem. Phys., 22, 15685–15702, 2022
https://doi.org/10.5194/acp-22-15685-2022-supplement

Atmospheric Chemistry and Physics
Open Access
EGU

Supplement of

Development and application of a multi-scale modeling framework for urban high-resolution NO_2 pollution mapping

Zhaofeng Lv et al.

Correspondence to: Huan Liu (liu_env@tsinghua.edu.cn)

Section S1. Urban heat island scheme

The Urban Heat Island effect refers to a phenomenon that the temperature of urban atmosphere and surface is higher than that of nearby rural areas, of which intensity can be quantified by using the temperature difference. UHI is caused by the thermodynamic effect of the special underlying surface structure induced by urbanization and the influence of human activities. In past decades, the intensity of UHI in Beijing has been increasing at a rate of 1.35 ℃ every decade, and has gradually expanded from within the 2nd Ring Road to the 6th Ring Road and its surrounding areas (Ge et al., 2016). When the UHI intensity is high, the circulation between urban and suburban areas will enhance the boundary layer height and turbulence intensity in urban areas, and reduce the concentration of primary pollutants such as NO_x which are easily affected by the local climate. After adding the UHI scheme to the model, the overestimation of the simulation can be reduced, and the simulation is more consistent with the observed concentration (Sarrat et al., 2006).

Here, based on the algorithm used in AERMOD (Cimorelli et al., 2005), we estimated the influence of UHI on turbulence in urban areas, especially in the afternoon (16:00-23:00), to reduce the over-predicted pollutant concentrations caused by the overestimation of atmospheric stability in this period. During this period, due to the large amount of anthropogenic heat generated by transportation, cooking and other human activities, as well as the gradual release of solar radiation stored by buildings in daytime, the UHI intensity in Beijing increase to the peak (Wang et al., 2017). In the calculation, we still regarded each road as a basic unit for the calculation, and first estimated the sensible heat flux $H_{\mathrm{u,UHI}}$ (W/m^2) caused by UHI and the height of the mixing layer $Z_{\mathrm{mix,c}}$ (m) formed by thermal turbulence. And then the mixing height Z_{mix}, convective velocity scale w^*, surface friction velocity u^*, and Monin-Obhukov length L_{MO} were recalculated based on AERMOD method (Cimorelli et al., 2005; EPA, 2019), as follows,

$$\begin{cases} H_{\mathrm{u,UHI}} = \alpha \rho c_{\mathrm{p}} \Delta T_{\mathrm{u-r}} u^* \\ Z_{\mathrm{mix,c}} = Z_{\mathrm{mix,ref}} (P/P_{\mathrm{ref}})^{0.25} \end{cases}$$

where, α is the empirical coefficient, with a value of 0.03. ρ is air density (kg/m^3) and calculated by air pressure and temperature. c_{p} is the specific heat capacity of air at constant pressure, with a value of 1004 J/kg·K. $\Delta T_{\mathrm{u-r}}$ is the temperature difference between urban and suburban areas, which is set with the value of 3℃ according to the observation of several meteorological ground observation stations and satellite remote sensing data (Wang et al., 2017). $Z_{\mathrm{mix,ref}}$ and P_{ref} are the reference boundary layer height and urban population, with values of 400 m and 2 million, respectively (Cimorelli et al., 2005). P is the total population of urban areas in the research region, with the value of 9.2 million in our study domain for 2020 based on the WorldPop dataset (Bondarenko et al., 2020).

Section S2. Vertical mixing scheme

Since the settings of vertical pressure layers in the CMAQ and the WRF model are same, the concentrations induced by non-vehicle sources provided by the CMAQ-ISAM model can be regarded as the background concentration at the top of the urban canopy layer (UCL). If the influence of

turbulence changes on the mixing of background concentration is not taken into account, the pollutant concentration at night stable boundary layer is easy to be significantly overestimated (Benavides et al., 2019). Therefore, we assumed that the concentration relationship between the top of UCL and the near surface is affected by atmospheric stability, local street canyons and building morphology.

In this study, based on the method proposed by Benavides et al. (2019), the ratio of wind speed between the near surface of the road and the top of surrounding buildings was used as a proxy parameter in the model to characterize the turbulence intensity which affects the vertical concentration mixing between the top of UCL and near surface. However, Benavides et al. assumed that the average wind speed in the street canyon was proportional to the angel between the top wind direction and the central axis of the road, and the logarithmic wind profile to was still used to represent the change of wind speed within UCL, resulting in the influence of the street canyon effect on vertical mixing of background concentration was not considered. In this study, when the grid receptor was located in the street canyon, the MLSCF scheme was used to describe the wind profile within UCL. Otherwise, the logarithmic wind profile was used to calculate the wind speed at the specified height. This parameter scheme mainly calculated the background concentration mixing ratio (fac_{bg}), which was multiplied by the background concentration provided by the CMAQ-ISAM model to estimate the background concentration at the specified height near the ground. Based on the estimated sensible heat flux (H_u, W/m^2) from the WRF model, convective boundary layer (H_u>0) and stable boundary layer (H_u<0) were distinguished, and the effect of building density around the receptor site on fac_{bg} was also considered, as follows:

$$\mathrm{fac_{bg}} = \begin{cases} 1 - F + F \times \dfrac{\mathrm{WS_{sfc}}}{\mathrm{WS_{bh}}}, & \mathrm{bd} > 0.1 \& H_u > 0 \\ \dfrac{\mathrm{WS_{sfc}}}{\mathrm{WS_{bh}}}, & \mathrm{bd} > 0.1 \& H_u \le 0 \\ 1 - 5\mathrm{bd} + 5\mathrm{bd} \times \dfrac{\mathrm{WS_{sfc}}}{\mathrm{WS_{bh}}}, & \mathrm{bd} \le 0.1 \& H_u > 0 \\ 1 - 10\mathrm{bd} + 10\mathrm{bd} \times \dfrac{\mathrm{WS_{sfc}}}{\mathrm{WS_{bh}}}, & \mathrm{bd} \le 0.1 \& H_u \le 0 \end{cases}$$

where, F=m+abs(0.25-bd), where m is an empirical parameter with value of 0.1. The transition value of H_u changed from 0.3 to 0 in this research compared with the Benavides's study in order to avoid the double-counting of impacts from the UHI effect.

Section S3. NO_x photochemical parameter scheme

The NO_x photochemical parameter scheme applied in this study includes two reactions:

$$\begin{cases} \mathrm{NO_2 + hv \rightarrow NO + O_3} \\ \mathrm{NO + O_3 \rightarrow NO_2} \end{cases}$$

Kim et al. compared two-reaction scheme with CB05 gas phase chemical mechanism by incorporated them into SinG model to estimate roadside NO_2 concentration, and found a similar results, while the computing time cost of two-reaction scheme was significantly less than that of the CB05 mechanism (Kim et al., 2018). Therefore, the simplified two-reaction scheme was incorporated into the model in

this study to characterize the NO_x photochemical process. During simulation, the NOx ($NO+NO_2$) emitted from vehicles is first regarded as an inert gas and only the primary concentration after diffusion is simulated. Then, assuming a photo-stationary equilibrium condition, the concentrations of NO, NO_2 and O_3 are calculated using the two-reaction scheme, as follows:

$$\begin{cases} [\mathrm{NO_2}] = (b - \sqrt{b^2 - 4c})/2 \\ [\mathrm{NO}] = [\mathrm{NO}]_\mathrm{b} + [\mathrm{NO_2}]_\mathrm{b} + [\mathrm{NO_x}]_\mathrm{d} - [\mathrm{NO_2}] \\ [\mathrm{O_3}] = [\mathrm{O_3}]_\mathrm{b} + [\mathrm{NO_2}]_\mathrm{b} + \zeta[\mathrm{NO_x}]_\mathrm{d} - [\mathrm{NO_2}] \\ b = k1/k2 + [\mathrm{O_3}]_\mathrm{b} + [\mathrm{NO}]_\mathrm{b} + 2[\mathrm{NO_2}]_\mathrm{b} + (1+\zeta)[\mathrm{NO_x}]_\mathrm{d} \\ c = ([\mathrm{O_3}]_\mathrm{b} + [\mathrm{NO_2}]_\mathrm{b} + \zeta[\mathrm{NO_x}]_\mathrm{d})([\mathrm{NO}]_\mathrm{b} + [\mathrm{NO_2}]_\mathrm{b} + [\mathrm{NO_x}]_\mathrm{d}) \end{cases}$$

where, $[NO_x]_d$ is the primary concentration of NO_x directly simulated by RLINE model when taken as an inert gas. $[NO]_b$, $[NO_2]$, and $[O_3]_b$ are the background concentrations of NO, NO_2 and O_3 from non-vehicle sources, respectively, which are provided by CMAQ-ISAM model. If the vertical mixing scheme is used in the hybrid model, $[NO]_b$, $[NO_2]$, and $[O_3]_b$ are derived by multiplying background concentrations from CMAQ-ISAM model with $\mathrm{fac_{bg}}$. The unit of concentrations in these formulas is mol/m^3. ζ is the ratio of NO_2 to NO_x in vehicle emissions, with a value of 0.2 (Valencia et al., 2018; Benavides et al., 2019). The reaction rates of the photolysis of NO_2 and the oxidation of NO were set to be *k1* and *k2* respectively, and calculated as follows (Hurley, 2005):

$$\begin{cases} k1 = 10^{-4} \times \delta \times \mathrm{TSR} \\ k2 = 9.24 \times 10^5 \times \exp(-1450/T)\,/T \end{cases}$$

$$\delta = \begin{cases} 4.23 + 1.09/\cos Z, & 0 \le Z \le 47 \\ 5.82, & 47 < Z \le 64 \\ -0.997 + 12(1 - \cos Z), & 64 < Z \le 90 \end{cases}$$

where, all parameters were from the WRF model. TSR is the total solar radiation (W/m^2). *Z* is the solar zenith angle (°). *T* is the ambient temperature (K).

Supplementary Figures

Figure S1. Spatial distribution of street canyon geometry in Beijing (© Microsoft). (a) Length of actual street canyon to the total street length, (b) Height to width ratio, (c) Length to height ratio and (d) Height symmetrical ratio.

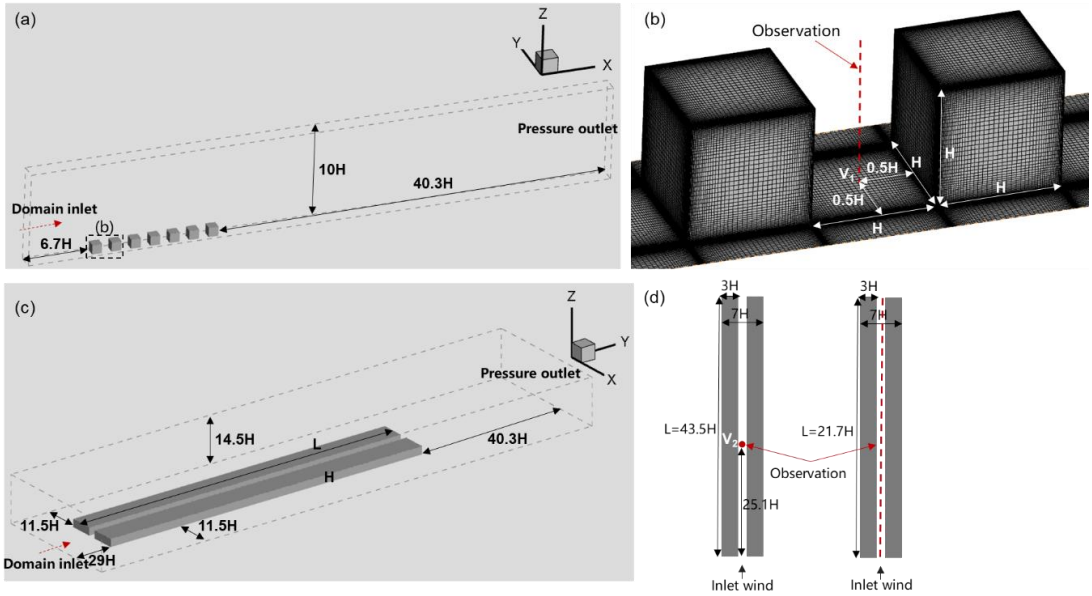

Figure S2. Computational domain and grid arrangement in CFD validation cases with the background wind being perpendicular (a-b) or parallel (c-d) to the axis of street canyons. In the first validation case (a-b), the vertical profiles of time-averaged velocity components (stream-wise velocity U and vertical velocity W) are measured at point V_1. In another validation case (c-d), the vertical (point V_2) and horizontal (z=0.11H) profiles of time-averaged stream-wise velocity U are measured.

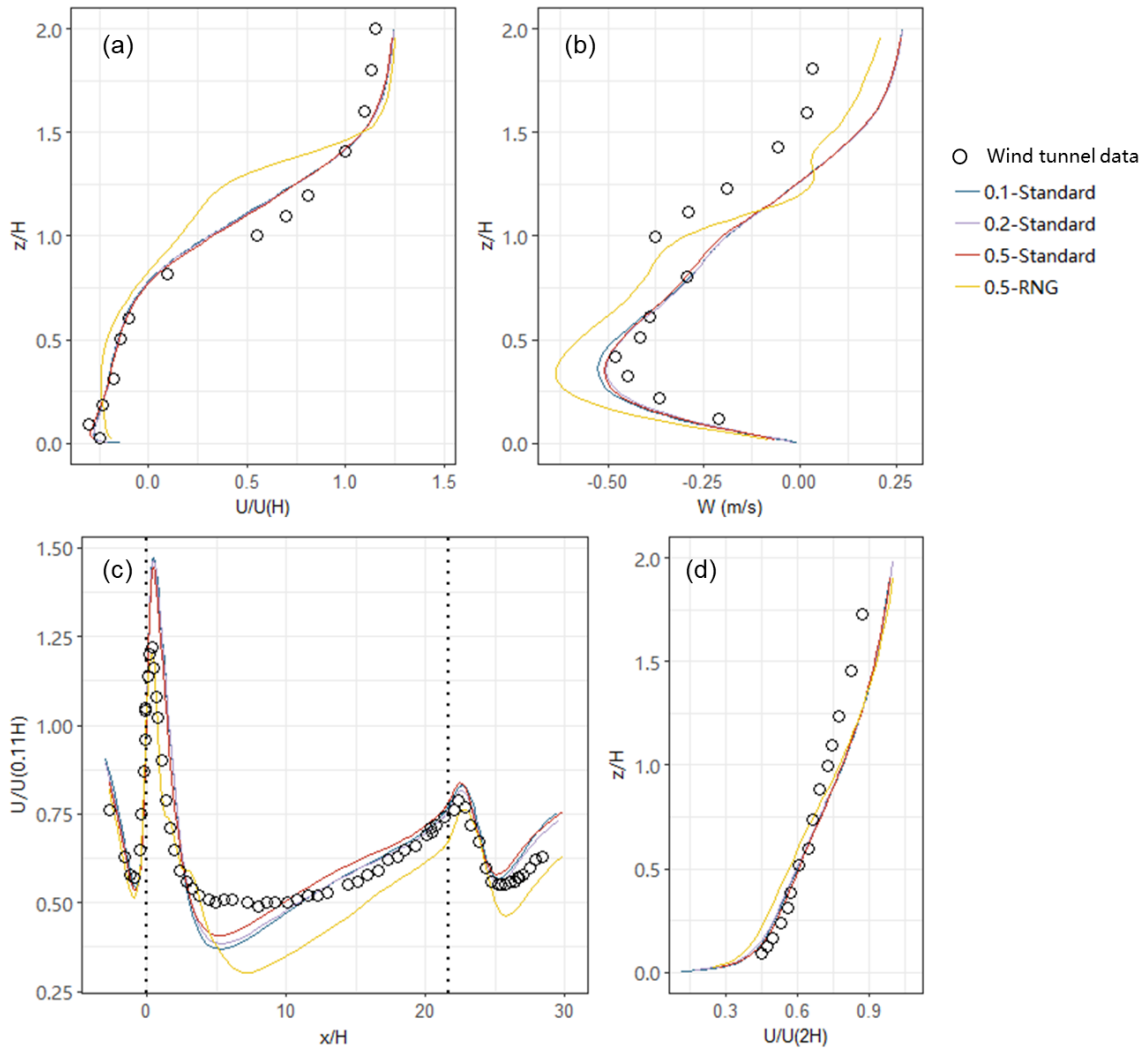

Figure S3. Model performances of CFD validation cases in street canyons perpendicular (a-b) or parallel (c-d) to the wind direction at the roof level. (a) Vertical profiles of U at point V_1; (b) Vertical profiles of W at point V_1; (c) Horizontal profiles of U at z=0.11H; (d) Vertical profiles of U at point V_2. In each validation case, three grid arrangement are tested, where the minimum sizes of hexahedral cells near wall surfaces are 0.1 m (fine grid), 0.2 m (medium grid) and 0.5 m (coarse grid) respectively. Moreover, the standard and RNG k-ε turbulence models are tested respectively.

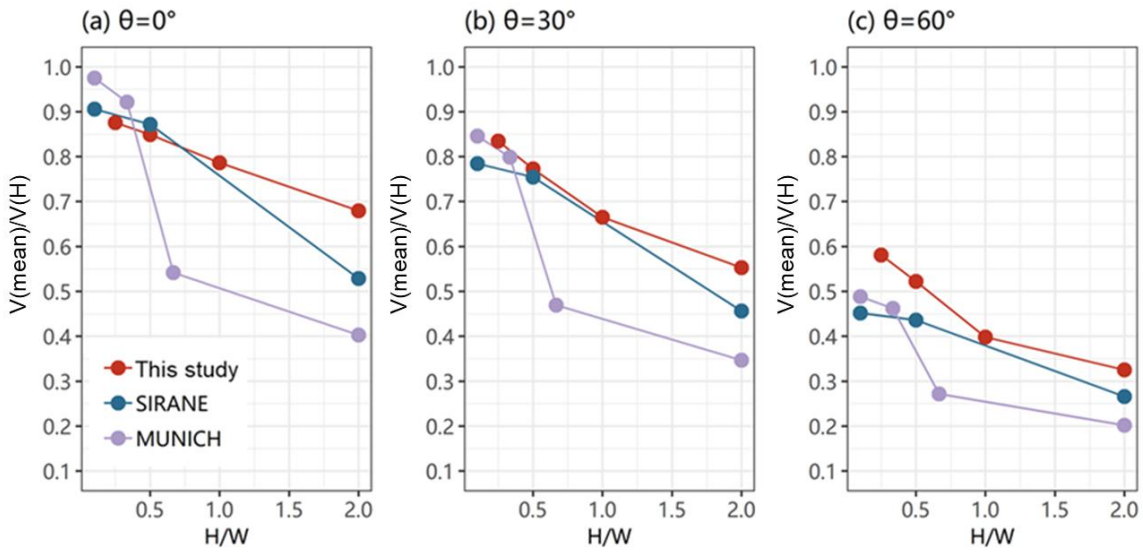

Figure S4. Comparison between the predicted wind speed in street canyons with different background wind direction and aspect ratio and other research results.

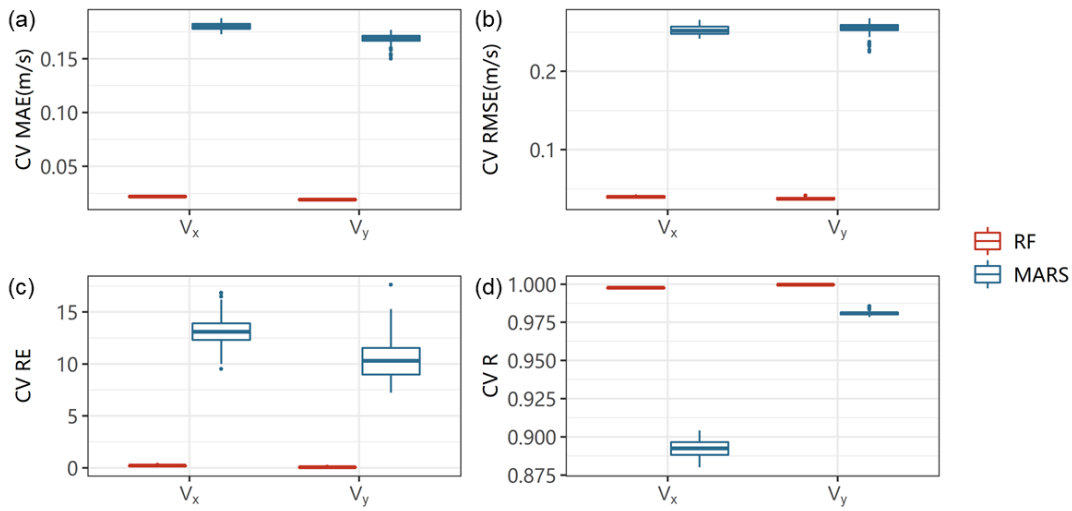

Figure S5. Model performance statistics of machine learning for $\boldsymbol{V_x}$ and $\boldsymbol{V_y}$ in street canyon. (a) MAE; (b) RMSE; (c) RE; (d) R.

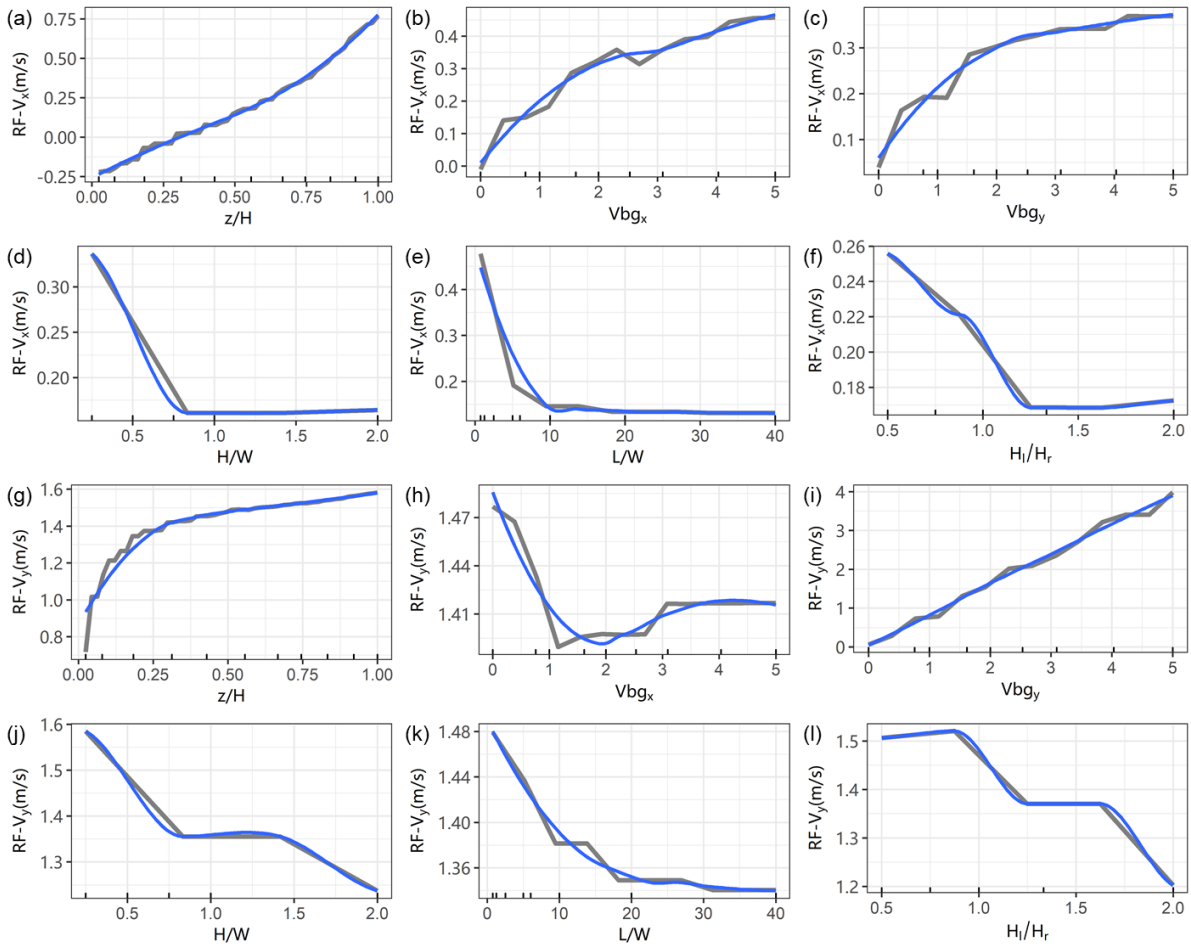

Figure S6. The partial dependence plots of each predictor variable in RF model for V_x (a-f) and V_y (g-l). The blue line stands for the smooth fitting curves. The labels above the x-axis shows deciles, minimum and maximum of the predictor variable.

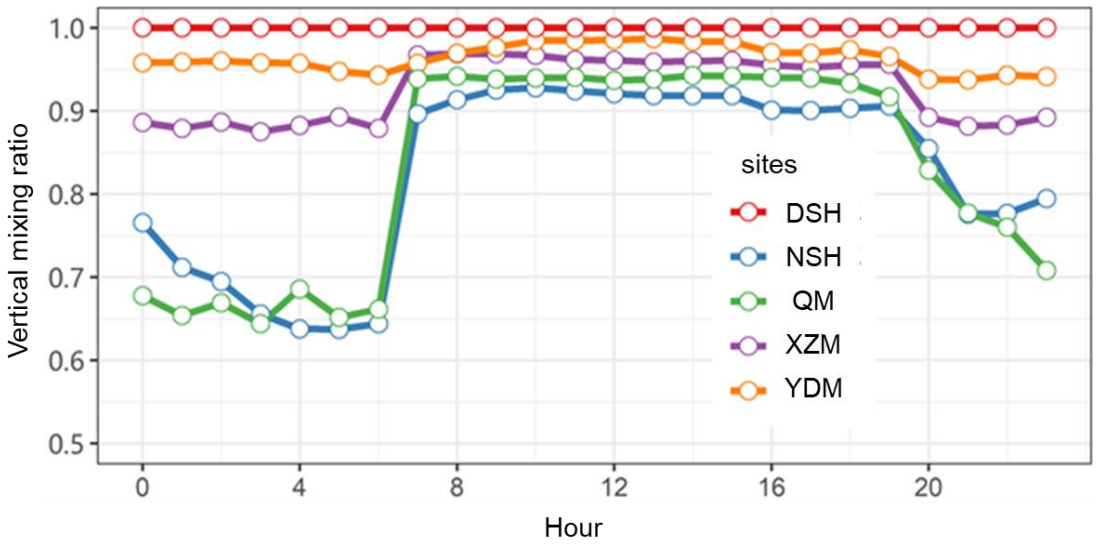

Figure S7. Diurnal variation of background concentration mixing ratio at roadside monitoring sites in Beijing in summer 2019. The vertical mixing ratio=concentrations near surface/at the top of UCL

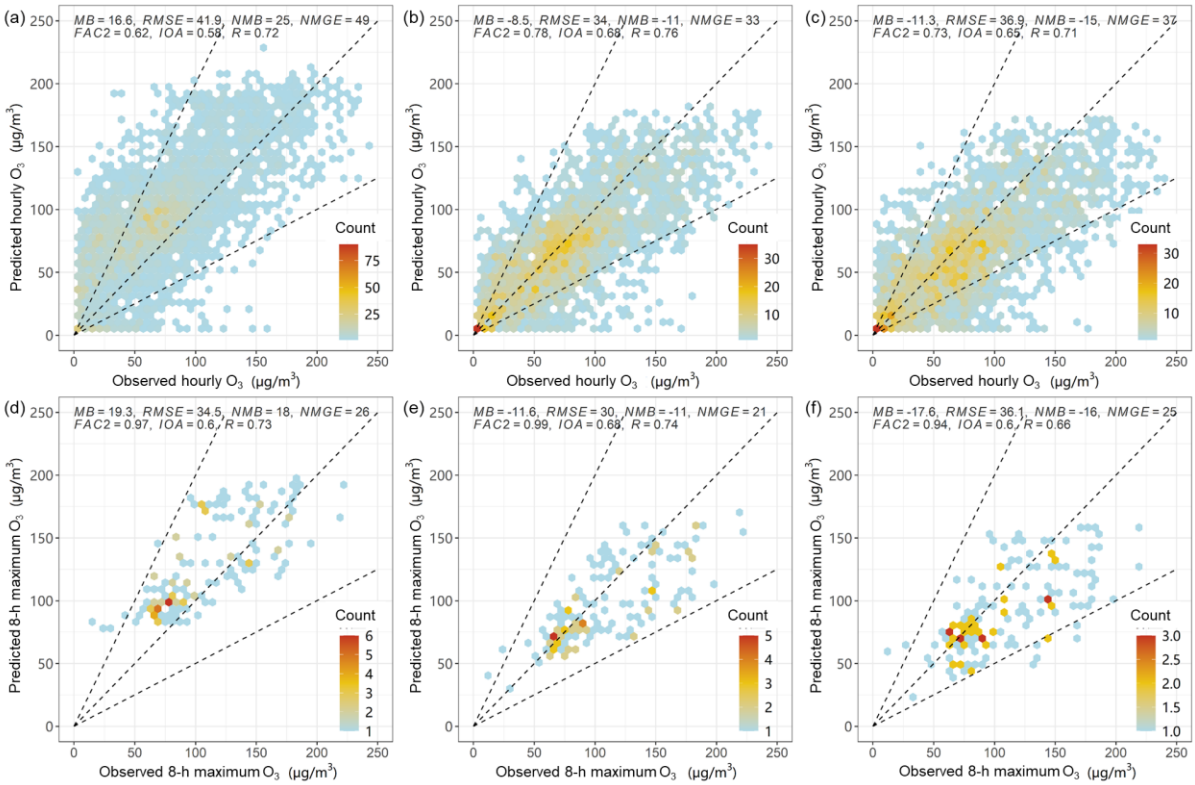

Figure S8. Observed and predicted hourly (a-c) or 8-h maximum averaged (d-f) O_3 concentrations from different models at near-road sites: (a, d) CMAQ model; (b, e) CMAQ-RLINE model; (c, f) CMAQ-RLINE_URBAN model.

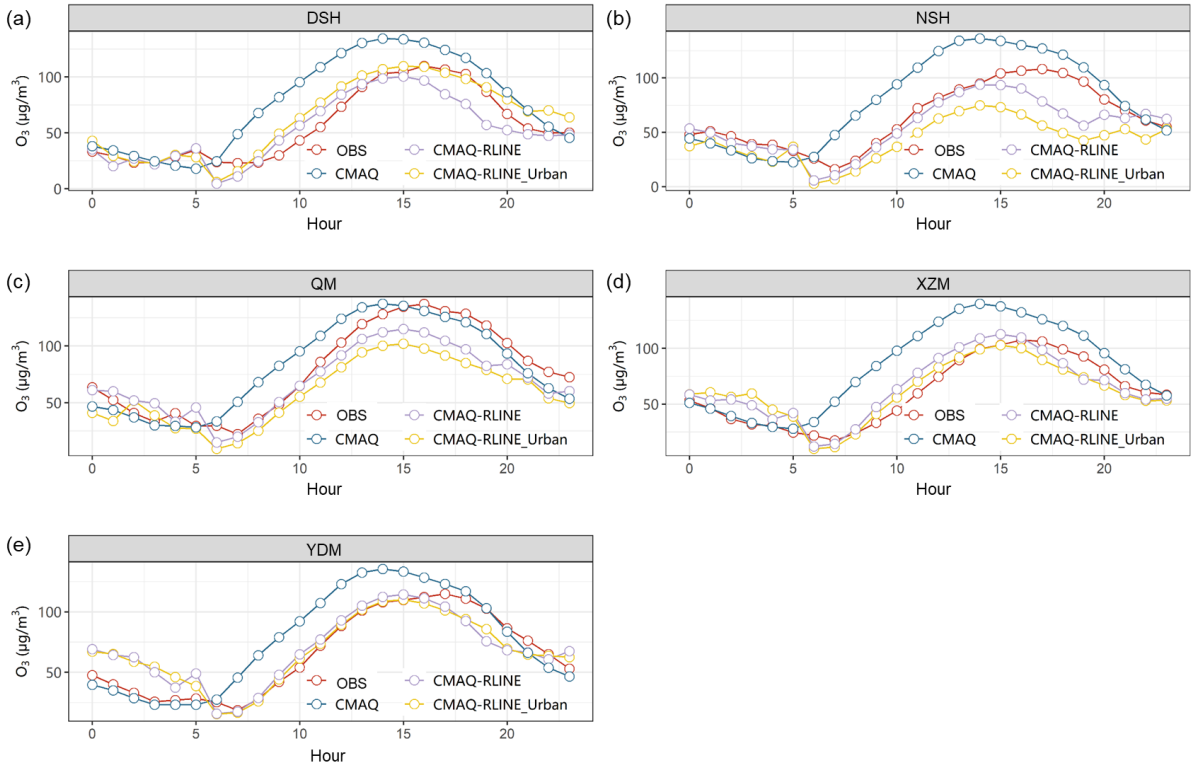

Figure S9. Diurnal variations of observed and predicted hourly averaged O_3 concentrations from different models at near-road monitoring sites: (a) DSH; (b) NSH; (c) QM; (d) XZM; (e) YDM.

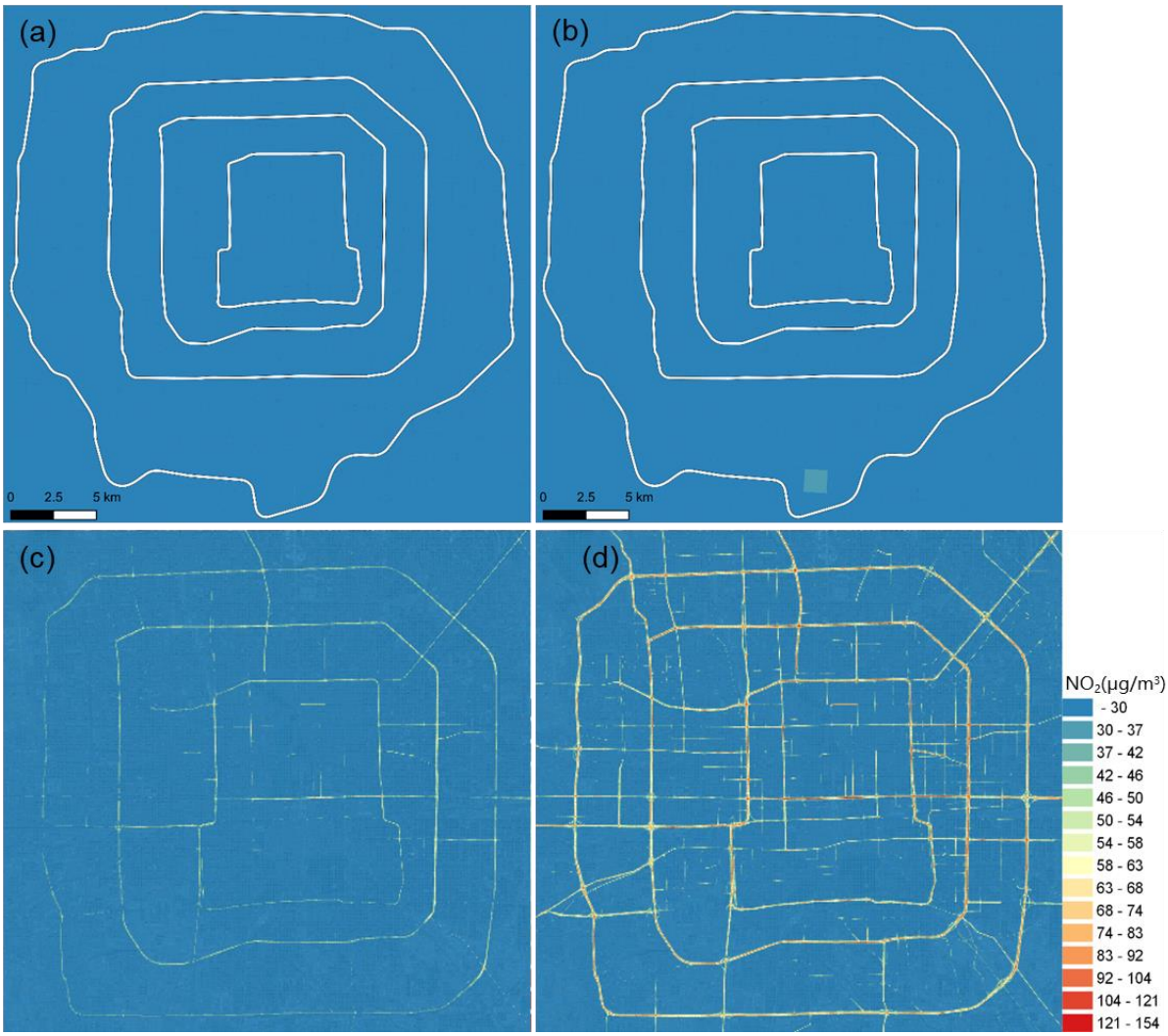

Figure S10. Spatial distribution of hourly averaged NO_2 concentrations from (a, b) CMAQ model and (c, d) CMAQ-RLINE_URBAN model at (a, c)12:00-13:00 and (b, d) 18:00-19:00.

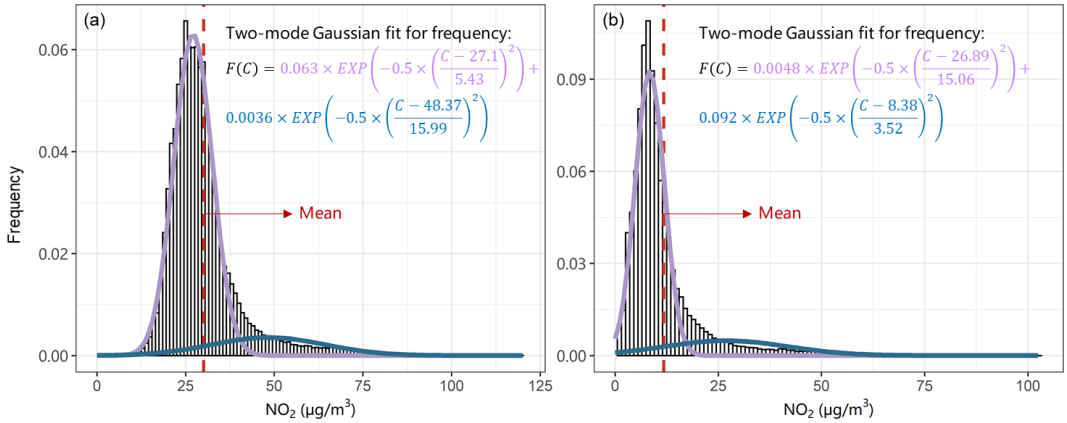

Figure S11. Frequency distribution of predicted monthly averaged NO2 concentrations from (a) all source and (b) only vehicles. Two-mode Gaussian models, which are shown by purple and blue curves, are used to fit for the distribution.

Supplementary Tables

Table S1. Model performance statistics for the velocity components in CFD validation cases.

Species	Mean Observation (m/s)	Mean Simulation (m/s)	FAC2	MFB (%)	NMSE (%)	R
Validation case with the perpendicular background wind						
u	-0.48	-0.50	1.00	-5	2	0.98
w	-0.37	-0.39	1.00	-4	5	0.58
Validation case with the parallel background wind						
u(L=21.7H)	0.68	0.73	1.00	-7	3	0.97
u(L=43.5H)	0.58	0.59	1.00	-1	0	0.99

Note: The coarse grid arrangement and standard k-ε turbulence model are used.
*MFB: Mean fractional

Table S2. Coefficients in V_x fitting of Multivariate Adaptive Regression Splines

Terms	Expression	Coefficients
1	Intercept	0.532
2	max(0.5-Vbg_x, 0)	-0.623
3	max(Vbg_x-0.5, 0)	0.111
4	max(2.5-Vbg_y, 0)	-0.131
5	max(Vbg_y-2.5, 0)	-0.010
6	max(0.5-H/W, 0)	2.315
7	max(H/W-0.5, 0)	-0.259
8	max(0.774-z/H, 0)	-0.812
9	max(z/H-0.774, 0)	2.774
10	max(2.5-Vbg_x, 0)×max(0.5-H/W, 0)	-1.103
11	max(Vbg_x-2.5, 0)×max(0.5-H/W, 0)	0.249
12	max(0.87-Vbg_x, 0)×max(0.774-z/H, 0)	0.481
13	max(Vbg_x-0.87, 0)×max(0.774-z/H,0)	-0.444
14	max(2.5-Vbg_x, 0)×max(z/H-0.774, 0)	-1.151
15	max(Vbg_x-2.5, 0)×max(z/H-0.774, 0)	-1.139
16	max(0.5-Vbg_y, 0)×max(0.5-H/W, 0)	-3.536
17	max(Vbg_y-0.5, 0)×max(0.5-H/W, 0)	0.028
18	max(0.5-H/W, 0)×max(0.774-z/H, 0)	0.897
19	max(H/W-0.5, 0)×max(0.774-z/H, 0)	0.664
20	max(Vbg_x-2.5, 0)×max(H_l/H_r-1.33, 0)×max(z/H-0.774,0)	-2.054
21	max(Vbg_x-2.5, 0)×max(1.33-H_l/H_r, 0)×max(z/H-0.774,0)	6.242

Table S3. Coefficients in V_y fitting of Multivariate Adaptive Regression Splines

Terms	Expression	Coefficients
1	Intercept	2.117
2	max(2.5-Vbg_y, 0)	-0.812
3	max(Vbg_y-2.5, 0)	0.624
4	max(1-H/W, 0)	0.455
5	max(H/W-1, 0)	-0.335
6	max(0.75-H_l/H_r, 0)	-0.081
7	max(H_l/H_r-0.75, 0)	-0.690
8	max(0.079-z/H, 0)	-14.220
9	max(z/H-0.079, 0)	0.200
10	max(0.5-Vbg_x, 0)×max(H_l/H_r-0.75, 0)	0.428
11	max(Vbg_x-0.5, 0)×max(H_l/H_r-0.75, 0)	-0.036
12	max(2.5-Vbg_y, 0)×max(H/W-1, 0)	0.152
13	max(2.5-Vbg_y, 0)×max(1-H/W, 0)	-0.265
14	max(2.5-Vbg_y, 0)×max(H_l/H_r-0.75, 0)	0.230
15	max(Vbg_y-2.5, 0)×max(H_l/H_r-0.75, 0)	0.109
16	max(2.5-Vbg_y, 0)×max(z/H-0.079, 0)	-0.090
17	max(2.5-Vbg_y, 0)×max(0.079-z/H, 0)	5.602
18	max(Vbg_y-2.5, 0)×max(z/H-0.226, 0)	0.536
19	max(Vbg_y-2.5, 0)×max(0.226-z/H, 0)	-2.361
20	max(1-H/W, 0)×max(H_l/H_r-0.75, 0)	0.480
21	max(H/W, 0)×max(H_l/H_r-0.75, 0)	-0.052

Table S4. Geometric characters for each monitoring site

Stations	*H*/*W*	bd	bh（m）	bhsd（m）	z_0（m）
DSH	0	0.01	4.97	1.68	1
NSH	0	0.13	19.61	31.96	1.06
QM	0.22	0.2	9.98	3.56	1.37
XZM	0.35	0.18	14.11	16.22	2.11
YDM	0	0.22	10.13	4.55	1.02

**H/W*, bd, bh, bhsd, and z_0 represent street canyon aspect ratio, average building height (m), height standard deviation (m) and plane density, respectively (Benavides et al., 2019).

Table S5. Model performances under different scenarios for each station

Sites	Scenario	MB	RMSE	NMB	NMGE	FAC2	IOA	*R*
	CMAQ	-15.6	33.4	-28	48	0.53	0.45	0.52
DSH	CMAQ-RLINE	28.2	63.1	51	69	0.73	0.20	0.50
	CMAQ-RLINE_URBAN	-6.2	28.5	-11	36	0.84	0.58	0.60
	CMAQ	-20.5	37.9	-33	50	0.53	0.12	0.30
NSH	CMAQ-RLINE	30.2	65.1	49	65	0.76	-0.12	0.33
	CMAQ-RLINE_URBAN	17.2	39.8	28	48	0.81	0.15	0.28
	CMAQ	-6.0	23.9	-14	42	0.64	0.45	0.59
QM	CMAQ-RLINE	20.4	55.2	47	68	0.8	0.11	0.47
	CMAQ-RLINE_URBAN	3.5	23.7	8	38	0.86	0.50	0.47
	CMAQ	-8.5	25.3	-18	44	0.61	0.36	0.54
XZM	CMAQ-RLINE	26.0	59.7	56	72	0.76	-0.06	0.41
	CMAQ-RLINE_URBAN	11.3	28.0	24	44	0.86	0.36	0.42
	CMAQ	0.6	25.5	1	44	0.66	0.43	0.58
YDM	CMAQ-RLINE	23.0	56.2	53	73	0.72	0.05	0.45
	CMAQ-RLINE_URBAN	5.4	25.0	12	39	0.86	0.50	0.50

*MB: Mean bias; RSME: Root mean squared error; NMB: Normalized mean bias; NMGE: Normalized mean gross error; FAC2: Fraction of predictions within a factor of two; IOA: Index of agreement; R: correlation coefficient.

Table S6. The performance of WRF model compared with observations.

Variables	Sample size	Observed Average	Simulated Average	MB	NMB	RMSE	*R*
WS10 (m/s)	732	2.5	3.7	1.2	46	1.9	0.6
WD10 (°)	456	190.4	169.0	-8.0	-4	49.5	0.4
T2 (°C)	742	25.8	29.0	3.2	12	3.5	0.9
RH (%)	741	64.3	50.4	-13.9	-22	17.4	0.9

*WS10: wind speed at the height of 10 m; WD10: wind direction at the height of 10 m; T2: Temperature at the height of 2 m; RH: Relative humidity; MB: Mean bias; RSME: Root mean squared error; NMB: Normalized mean bias; R: correlation coefficient.

Reference

Benavides, J., Snyder, M., Guevara, M., Soret, A., Pérez García-Pando, C., Amato, F., Querol, X., and Jorba, O.: CALIOPE-Urban v1.0: coupling R-LINE with a mesoscale air quality modelling system for urban air quality forecasts over Barcelona city (Spain), Geosci. Model Dev., 12, 2811-2835, 10.5194/gmd-12-2811-2019, 2019.

Bondarenko, M., Kerr, D., Sorichetta, A., and Tatem, A.: Census/projection-disaggregated gridded population datasets for 189 countries in 2020 using Built-Settlement Growth Model (BSGM) outputs, 2020.

Cimorelli, A. J., Perry, S. G., Venkatram, A., Weil, J. C., Paine, R. J., Wilson, R. B., Lee, R. F., Peters, W. D., and Brode, R. W.: AERMOD: A dispersion model for industrial source applications. Part I: General model formulation and boundary layer characterization, Journal of applied meteorology, 44, 682-693, 2005.

EPA: AERMOD model formulation and evaluation[R]. EPA-454/R-19-014. US Environmental Protection Agency, Research Triangle Park, NC., 2019.

Hurley, P.: The air pollution model (TAPM) version 3. Part 1. Technical description. Aspendale, Vic, 2005.

Kim, Y., Wu, Y., Seigneur, C., and Roustan, Y.: Multi-scale modeling of urban air pollution: development and application of a Street-in-Grid model (v1. 0) by coupling MUNICH (v1. 0) and Polair3D (v1. 8.1), Geoscientific Model Development, 11, 611-629, 2018.

Sarrat, C., Lemonsu, A., Masson, V., and Guédalia, D.: Impact of urban heat island on regional atmospheric pollution, Atmospheric environment, 40, 1743-1758, 2006.

Valencia, A., Venkatram, A., Heist, D., Carruthers, D., and Arunachalam, S.: Development and evaluation of the R-LINE model algorithms to account for chemical transformation in the near-road environment, Transportation Research Part D: Transport and Environment, 59, 464-477, https://doi.org/10.1016/j.trd.2018.01.028, 2018.

Wang, K., Jiang, S., Wang, J., Zhou, C., Wang, X., and Lee, X.: Comparing the diurnal and seasonal variabilities of atmospheric and surface urban heat islands based on the Beijing urban meteorological network, Journal of Geophysical Research: Atmospheres, 122, 2131-2154, 2017.